$$\boldsymbol{H}_{total} = \sum_{ij}(\boldsymbol{H}_{ij}^{(+)} + \boldsymbol{H}_{\boldsymbol{ij}}^{(-)})$$

The direction of the field is defined by the sign of the elementary charge $Q_ij^{((+/-))}$and direction of the vector pointing towards the point of interest $\boldsymbol{d}\_ij^{((+/-))}$.

$$\boldsymbol{H}_{total} = \sum_{ij}(\frac{Q_{ij}^{(+)}}{\left|\boldsymbol{d}_{ij}^{(+)}\right|^2} * \frac{\boldsymbol{d}_{ij}^{(+)}}{\left|\boldsymbol{d}_{ij}^{(+)}\right|} + \frac{Q_{ij}^{(-)}}{\left|\boldsymbol{d}_{ij}^{(-)}\right|^2} * \frac{\boldsymbol{d}_{ij}^{(-)}}{\left|\boldsymbol{d}_{ij}^{(-)}\right|})$$

- In “Coulombian Model” of magnetic field calculation, volume magnetization is replaced with surface charges
- For numerical calculation continuous charge distribution is approximated by an array of point charges with separation ΔL
- The density of point charges has to be selected appropriately compared to the distance d to the point where the field is calculated
- For good approximation

This approach has been done by Wolfram [2] which explains some of the results and the obstacles came across by the results of not taking a high enough density cut for the integration leaving numerical artifacts.

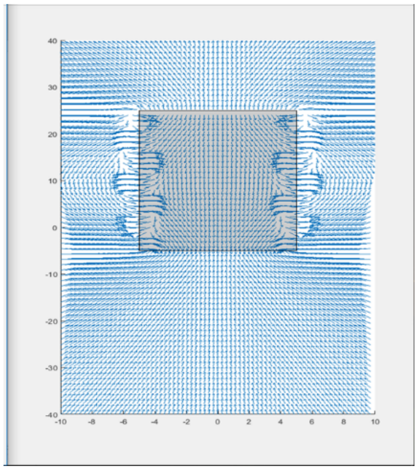

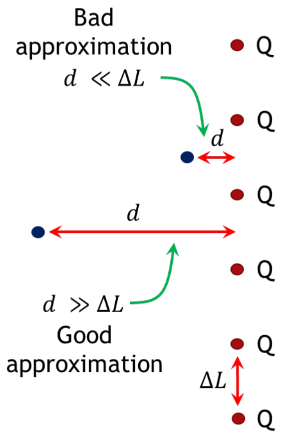

- In “Coulombian Model” of magnetic field calculation, volume magnetization is replaced with surface charges

- For numerical calculation continuous charge distribution is approximated by an array of point charges with separation ΔL
- The density of point charges has to be selected appropriately compared to the distance d to the point where the field is calculated
- For good approximation

Applications:

The CEM uses many spin resonance techniques. One of them is implanted 8Li ion beta detected NMR that is used as a probe of local magnetic field. NMR resonant frequency is the measure of local magnetic field. Experimentally measured strength of local magnetic field in the vicinity of YIG layer will be compared with the results of the numerical calculation of magnetic field of the YIG layer

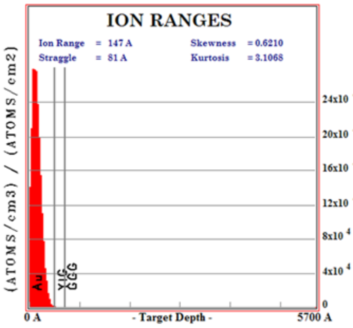

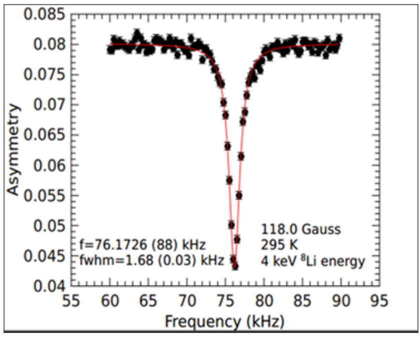

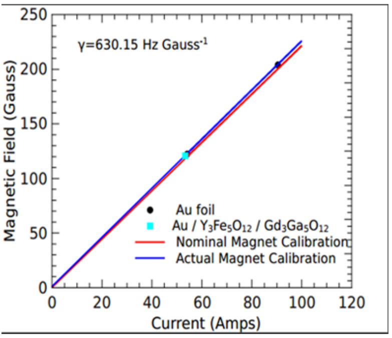

Conclusion:

Introduction to magnetism on the microscopic scale – investigation of a classic system, a uniformly magnetized slab using numerical finite element modeling done with MatLab. Investigation of the limitations created of a numerical simulation, the pitfalls of finite element analysis and where the models might fail at small distances. Future development of a more sophisticated model, involving more complicated shapes or magnetization which varies in time. Ultimately application of this model to the research problems relevant to the OSU CEM

Acknowledgments:

Denis Pelekhov, Sarah Dunsiger, Shane White, Bill Ruane, Chi Zhang

Sources:

[1] Magnetism and Magnetic Materials, J.M.D. Coey

[2] http://blog.wolfram.com/2013/08/27/musing-about-rectangular-bar-magnets/

Characterizing Magnetic Properties of Micro-Scale $Nd_2Fe_{14}B$ and $SmCo_5$ Particles Using Cantilever Magnetometry

Laura Jennings, Bill Ruane, Shane White, P. Chris Hammel
National Science Foundation, Center for Emergent Materials, The Ohio State University

ABSTRACT

On a microscopic scale, the properties of Samarium Cobalt ($SmCo_5$) and Neodymium Iron Boron ($Nd_2Fe_{14}B$) behave differently than in bulk measurements. With the use of a cantilever, the small signals of these magnets can be measured in order to characterize the particles. Through cantilever magnetometry, when sweeping an applied external field, a Frequency vs. Field graph can be constructed that allows for the measurement of moment and coercive field. The moment of a 5.4-micron diameter samarium cobalt particle was measured to be $3.1 \times 10^{-9} emu$. For another Samarium Cobalt sample, the moment was measured to be $1.0351 \times 10^{-9} emu$ with a coercive field of 17587 G. Through this experiment, these results were evaluated and future directions were advised.

I. Introduction

Micro and nano-scale magnetic systems are becoming increasingly important in today's technology. Thus, a better understanding of magnetic systems on this scale is needed. A cantilever with a micro-magnetic particle provides the ability to measure the small signal sizes of these systems. A cantilever of this type can be used to probe local characteristics of other magnetic materials once the magnetic properties (moment and coercive field) of the particle are known. One example being Scanning Ferromagnetic Force Microscopy (sFMRFM), which uses the cantilever with the particle as a probe. However, the scale of probing other materials is set by the size, coercivity, and moment of the probe, making it necessary for such values to first be exposed by cantilever magnetometry. These developments yield insight into properties that are influential for improving data processing and storage capabilities.

In this type of cantilever magnetometry, a particle is glued to the tip cantilever and when an AC voltage is applied, the oscillations/deflection of the cantilever can be recorded using laser interferometry. This method uses a laser to measure the frequency of oscillation. When frequency is graphed as a function of field, the coercive field is shown and it can lead us to derive the magnetic moment of that particular magnet. Cantilevers are extremely sensitive to small torques and laser interferometry can detect the smallest deflection of the tip, allowing us to measure such microscopic properties. On this micro-scale, signal outputs are extremely small. Because of this, the cantilever is situated on a piezoelectric transducer, which works to drive the cantilever into motion.

Samarium Cobalt ($SmCo_5$) and Neodymium Iron Boron ($Nd_2Fe_{14}B$) are both rare earth magnets. Neodymium Iron Boron is the strongest commercially available permanent magnet for the smallest volume [3, 5]. This makes it a desirable magnet to work with on a small scale and within any electronic devices or machines. While $Nd_2Fe_{14}B$ is stronger than Samarium Cobalt, their magnetic strength overlaps at certain temperatures. For higher temperatures, Samarium Cobalt is stronger and on average, it also has a higher coercivity making it more effective in larger magnetic fields before demagnetizing [4, 5]. While both of these properties are useful, $SmCo_5$ is also more expensive, leaving it to be less widely used [5]. However, all of these attributes are on average for macro-sized samples of the magnets, not on the micro-scale.

II. Theory

The cantilever magnetometry performed was based on the interaction of the applied external magnetic field, H, with the magnetic moment m, of the particle.

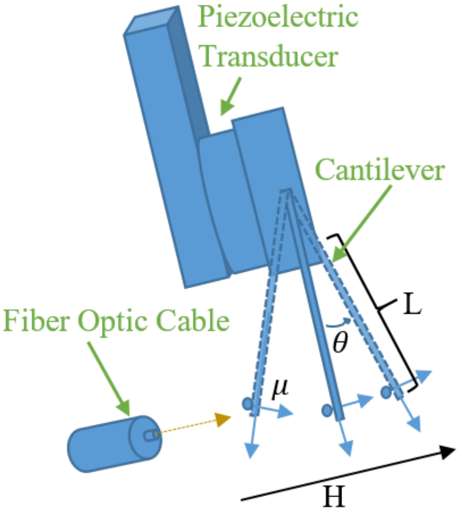

FIG 1. *Schematic diagram of the motion of the cantilever when an external field **H** is applied. The cantilever will be deflected to an angle **θ**, and moment **m** will remain normal to the cantilever of length **L**.*

The relationship between these is the torque that is created, given by $\tau = m \times H$ or $\tau = mH\sin\theta$ where θ is the angle between resting position and the deflection. For very small values of θ we can consider $\sin(\theta) \approx \theta$. When considering all the forces working on the system, we can construct the following equation of motion:

$$\text{(Eq.1) } I\alpha = -mH\theta - kL^2\theta$$

We know that $I\alpha$, is equal to the net torque consisting of torque on the moment caused by the external magnetic field and a cantilever restoring force. This restoring force takes a similar form to the spring restoring force, where k is the force constant of the cantilever and L is the effective length (total length/1.38) of the oscillating cantilever.

$$\text{(Eq. 2) } I\alpha = -K_{eff}\theta$$

A variable K_{eff} has been introduced to simplify the form of *Eq. 1*, and is a measure of the strength of the restoring torque. The solution to *Eq. 2* is simple harmonic motion where the angular frequency is given by:

$$\omega^2 = \frac{-K_{eff}}{I}$$

From this, we are able to obtain a relationship between the moment, m, of the magnetic particle based on the measured frequency of oscillation, f.

$$\text{(Eq. 3) } m \approx \frac{4\pi\sqrt{kL^2}}{\sqrt{I}}\frac{df}{dH}$$

Above, the magnetic moment, m, is a function of its predefined constants multiplied by $\frac{df}{dH}$, the slope of the fit to the Frequency vs. Field graph.

The coercive field can be found through the Frequency vs. Field graph. The coercive field is the field in which the particle becomes demagnetized. This can be seen on the graph by the dramatic change/jump in the field.

II. Methods

The first step in conducting cantilever magnetometry was gluing a magnetic particle to a silicon nitride cantilever. In order to obtain the sample of Samarium Cobalt, particles were shaved off of a larger source. Using a file, the oxidized layer of the cylinder-shaped magnet was filed off until samples of the metallic surface could then be shaved off. The Neodymium Iron Boron particles used came in the shape of spheres that did not need to be cut or shaved down. A clean glass slide positioned on top of a magnet was used to pick up a sample of particles. Only a small sample was needed in order to reduce clumping of the particles. After Stycast was mixed, a glass needle deposited the glue onto the cantilever tip. The same needle was then used to place a single magnetic particle on the cantilever. All glued cantilevers were then placed in nitrogen box to prevent oxidation of the magnet.

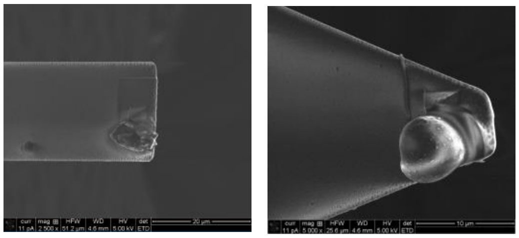

FIG 2. *Left: Triangle Silicon Nitride cantilever with ~5 micron Neodymium Iron Boron glued particle, Right: Rectangle Silicon Nitride cantilever with ~10 micron Samarium Cobalt glued particle*

The glued cantilever was then placed inside of a magnetometer, which works to hold the cantilever within the external magnetic field, as well as directly on top of a fiber optic cable. This fiber optic cable is the pathway for the laser to detect the motion of the cantilever tip. In order to assure contact with the piezoelectric transducer and the location of the cantilever above the cable, a magnetometer was redesigned.

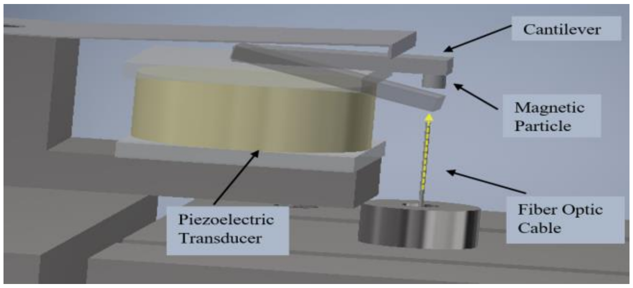

FIG 3. *Schematic of the glued cantilever situated inside the magnetometer above the fiber optic cable and piezoelectric transducer.*

Improvements in the redesign included movement in the x and y directions of the stage holding the cable, and positioning the cantilever clamp directly on the sapphire plate on top of the piezoelectric disc. This will decrease some noise in the output signal that was previously caused by the recording of unwanted vibrations. These vibrations were possibly caused by too long of a distance between the location of the piezo and the cantilever clamp, which was changed in the redesign.

Once the cantilever was situated, the entire device was locked into a vacuum and placed into an external, perpendicular, magnetic field. An AC voltage, attached to the piezo disc, was applied in order to prompt the cantilever oscillation. Values for Frequency, Amplitude, and Voltage were recorded. This was then repeated for a number of Field steps from -2 T to 2 T. The Frequency vs. Field relationship shown by *Figure 4* is the most important in determining the coercivity and the magnetic moment of the particle. Using *Equation 3,* magnetic moment was calculated. The coercive field was then found at the point where the magnetic field spikes and switches.

III. Results and Discussion

Laser interferometry was used to record the frequency of an oscillating cantilever with a glued particle on its tip. The frequency was then measured as a function of field, allowing us to extract the magnetic moment, m, of the particle through *Equation 3*. The graph also shows the coercive field where the particle becomes demagnetized. In addition to measuring a value for magnetic moment, the theoretical magnetic moment for the particle's volume was calculated in order to make a comparison. The theoretical moment can be found by:

$$m = 4\pi M_s \times (\frac{4}{3}\pi r^3)$$

In this equation, $4\pi M_s$ stands for saturation magnetization of the measured particle, and r is the radius. This theoretical value yields the total moment of the particle. The saturation polarization of Samarium Cobalt is 1.05T [1] and 1.3T for Neodymium Iron Boron. The calculated values for theoretical moment were $71.0 \times 10^{-9} emu$ for a 5.4-micron diameter $SmCo_5$ particle and $176 \times 10^{-9} emu$ for a 6.8-micron diameter $Nd_2Fe_{14}B$ particle.

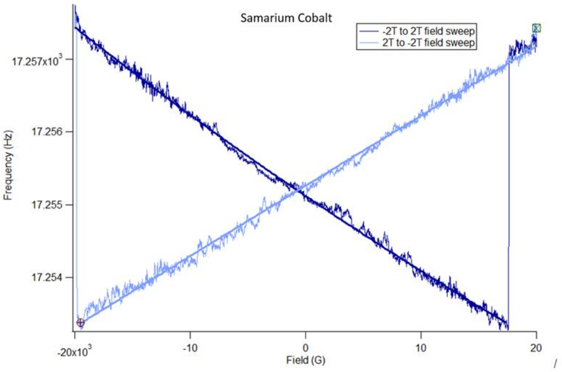

FIG 4. *Frequency vs. Field graph of Samarium Cobalt from -2T to 2T and 2T to -2T Field sweep. The slope of the fitted line of the data has a slope of* df/dH and the spike in the data shows the coercive field.

Due to time constraints, the only particles measured were Samarium Cobalt. Two field sweeps were successfully measured in a microscope with the capability to measure from -2T to 2T. This 3-micron Samarium Cobalt particle had a measured moment of $1.0351 \times 10^{-9} emu$. The coercive field, shown by *Figure 4*, was 17587 G. This information is important to know for further experiments in order to know what field strength the moment can withstand.

With the newly designed magnetometer, two more sweeps were successfully made from -2000G to 2000G. Although the full -2T to 2T range could not be reached, thus not reaching the coercive field, the data yielded for the 5.4-micron particle measured a moment of $3.1 \times 10^{-9} emu$. While a better approximation could be found with the larger field range, there was sufficient data to fit a slope of the Frequency vs. Field graph.

The measured moment for both of these $SmCo_5$, particles are substantially lower than the theoretical value. Magnetically dead regions within the particles may have caused this discrepancy.

A future goal is to be able to measure the moment and coercive field of the Neodymium Iron Boron particles that were glued. These particles are spherical and have a more uniform geometry that could yield better results than the irregular Samarium Cobalt. The difference in these shapes can be seen in *Figure 2*.

After attaining desired results, a Focused Ion Beam (FIB) will be used to shave down the glued particles. The $SmCo_5$ particles are very nonuniform in shape as they were shaved from a larger source, and the $Nd_2Fe_{14}B$ particles are spherical. The FIB turns the particles into cube-shaped pieces. This is done through shooting high beam current gallium ions at the surface. The interaction will cause a sputtering off of the edges of the material [2]. The measurements could then be redone in order to see if there is a change in measured magnetic moment. While this will create a more geometric shape, there is a possibility of degrading the coercive field of the particle. The use of the FIB will also be useful in sFMRFM where it is important to have a small and well-defined shape in order to model and predict the interaction of this probe with another magnetic material.

V. Conclusions

Overall, the magnetic moment of Samarium was measured from the fit of the Frequency vs. Field graphs of two different sized particles. These values were approximated to be $1.0351 \times 10^{-9} emu$ and $3.1 \times 10^{-9} emu$. These measured moment was then compared to the particle's expected theoretical moment. Differences in these values may have been caused by magnetically dead regions within the glued micro-scale magnet. In addition, the coercive field, 17587 G, of the first particle was extracted from this graph. There are necessary further steps to be taken in these measurements such as measuring the moment and coercive field of Neodymium Iron Boron and using the Focused Ion Beam to reshape the Samarium Cobalt particles. After this is done, the cantilevers can be used as a mechanism for probing the characteristics of other micro-scale magnets and measure local properties.

VI. Acknowledgments

Financial support awarded from the National Science Foundation through the Center for Emergent Materials at The Ohio State University.

VII. Footnotes, Endnotes and References

[1] Adler, E., & Sattler, W. Magnetization behavior of sintered SmCo5 hard magnetic material. Retrieved July 21, 2016, from http://www.sciencedirect.com/science/article/pii/0304885380903625

[2] Introduction: Focused Ion Beam Systems. Retrieved July 21, 2016, from http://www.fibics.com/fib/tutorials/introduction-focused-ion-beam-systems/4/

[3] Introduction to Neodymium Magnets. Retrieved July 21, 2016, from http://www.ndfeb-info.com/

[4] SmCo Magnet. Retrieved July 21, 16, from http://www.china-magnet.net/smco.html

[5] Magnet Guide and Tutorial. Retrieved July 21, 16, from http://www.allianceorg.com/pdfs/Magnet_Tutorial_v85_1.pdf

Surface Photovoltage Spectroscopy of a Dual Polarity Two-Dimensional Semiconductor

Maranda Reed, Thaddeus Asel, Geoffrey Foster and Dr. Leonard Brillson

Center of Emergent Materials at The Ohio State University

Abstract

This investigation is focused on the study of 2D Methyl-Terminated Germanane electronic properties as it pertains to defect detection and characterization. The study of germanane is of interest because it is a 2D direct bandgap semiconductor which has applications in optoelectronics. $GeCH_3$ was found to have a possible duality in conduction response when put under testing using surface photovoltage spectroscopy. The implications of this finding can impact material synthesis.

Background and Introduction

There are three major classifications of solid materials: insulators, conductors and semiconductors. A semiconductor is a type of solid material that can partially conduct current. The conductivity of a semiconductor is between that of an insulator, which has little conductivity, and a conductor, which is fully conductive. Semiconductor structure has a fully occupied valence band and an unoccupied conduction band separated by a bandgap with the midpoint called the Fermi level. The valence and conduction band are continuous bands of energy that occur because atomic orbitals of similar energy don't overlap. The differentiating factor between insulators, conductors, and semiconductors is how large the separation of band energies between the valence and conduction band or how wide is the bandgap. In insulators, the bandgap is very wide therefore the electrons are mostly unable to jump from the valence to the conduction band. In conductors, the two bands overlap, so that valence electrons require almost no energy to enter the conduction band, allowing current to flow freely. According to band theory, at ordinary temperatures, electrons in semiconductors having enough energy can jump across their bandgap to reach the conduction band.

The electrons' ability to jump from the valence to the conduction band is based on quantum mechanics which states that electrons will jump energy states in quantized steps when they absorb a specific energy. For example an upward transition (ground to an excited state) requires an absorption of a photon of a certain energy. If the electron were hit with a photon of lesser or greater energy, it would not move. The energy required for an electron to transition from the valence to the conduction band, specific to each material, is called the bandgap energy. When the band gap energy is met, the electron is excited into a free state, and can therefore participate in conduction. Defects present in semiconductors occur when the crystal lattice has imperfections so that electrons can get excited to a state within the bandgap. The problems that these defects present are numerous; for example, they decrease mobility of electrons when they get stuck in defect states. As a result of the lowered mobility, the speed of the electrons decreases, which slows down the device its powering. Semiconductors are essential to the creation of electronic devices like the transistor, diodes, integrated circuits and microchips. The purpose of this research is to identify and characterize defects within the bandgap of semiconductor material. Then to relate these defects states to the sample structure in order to develop better means of growing defect free materials.

Pervious research related to the work includes in surface photovoltage theory, experiment, and application by L. Kronik and Y.Shapira. Experimentation in 2D materials shown with MoS_2 by Kapildeb Dolui, Ivan Rungger, and Stefano Sanvito. Also, properties of methyl-terminated germanane by Shishi Jiang, Sheneve Butler, Elisabeth Bianco, Oscar D. Restrepo, Wolfgang Windl, and Joshua E. Goldberger.

Methods: Surface Photovoltage Spectroscopy

I. Principles of Surface Photovoltage Spectroscopy

The method used to detect defects in the bandgap was surface photovoltage spectroscopy (SPS). This method relies on the unique properties of surfaces and the photovoltaic effect. The photovoltaic effect is the creation of electron flow in a material upon exposure to light. Unlike the photoelectric effect which ejects electrons out of the material, the electrons under the photovoltaic effect remained contained in the material. This is an important distinction because the released carriers are now able to move freely leaving behind holes, which act as positively charged carriers. At the surface of materials the ideal periodic crystalline structure, that is present in the bulk of the solid, is disrupted. The structure at the surface reforms itself to the lowest energy configuration. This reconstruction can lead to the formation of localized states that induce a charge between the surface and the bulk crystal in order to create a thermal equilibrium. This exchange at interfaces and surfaces creates a small electric field which changes the electric potential at the surface that differs from the bulk. [1]

There is now an excess of charge on the surface of the material which results in band bending. In an n-type system, bands bend downward because the excess of negative charge repels electrons occupying the conducting band and attaches holes from the valence band. Figure 1 (a) depicts charge occupying a narrow range of bandgap energies on the surface of the material that is hit by a photon. If that photon contains a minimum energy for an electron to leave the "surface state" can hop into the conduction band where electric fields in the band bending region repel it into the bulk. The charge at the surface is now smaller than it was before so less repulsion is experienced by the conduction and valence band so that band bending lessens (second diagram in Figure 1). The Fermi level rises because the distance between it and the conduction band must remain constant in the semiconductor bulk. Also by definition the Fermi level is the energy where there is a 50% probability of finding an electron, so that with electrons depopulating the localized surface state, the 50% probability energy shifts. Figure 1 (b) depicts the opposite occurrence, an electron is excited from the valence band to the localized surface state which result in an increase in band downward bending. If almost all charge at the surface is removed with photons at the

---

[1] Leeor Konik and Yoram Shapira "Surface photovoltage spectroscopy of semiconductor structures: at the crossroads of physics, chemistry and electrical engineering"

bandgap energy, the bands almost completely flatten just as they are in the bulk. In a p-type system band bending is depicted as upward band bending with a depletion of negative charge at the surface. The change in Fermi level corresponding to a change in work function is measured as the contact potential difference (CPD). SPS consists of the semiconductor's work function plotted as a function of incident photon energy. The photon energy range is broad covering energies significantly above and below the band gap energy.

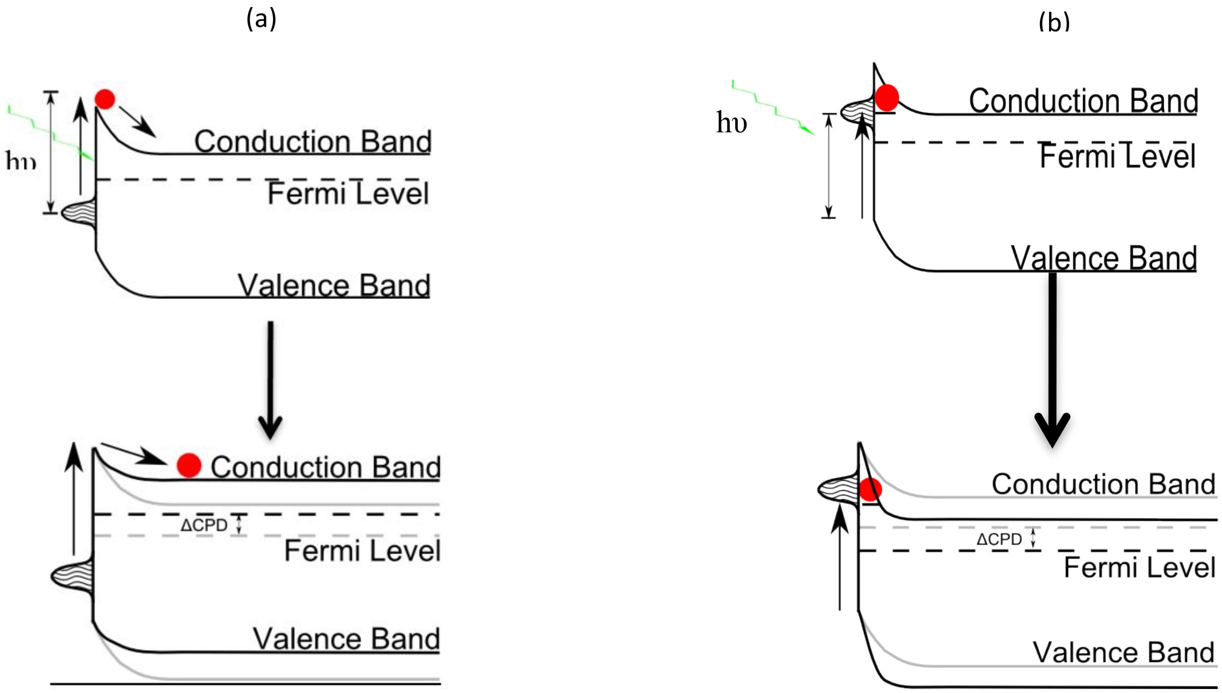

Figure 1: Schematic N-Type Semiconductor Bands diagrams: (a) Depict band bending, the excitation of electrons from a surface state into the conduction band (depopulating the state), and the resulting flattening of the band bending regions (b) Excitation of electrons from the valance band to the surface state (populating the states) and the resultant deepening of the band bending.

II. Experimental Procedure

Prior to taking SPS data, the experimental process for collecting data begins with two scans—Atomic Force Microscopy (AFM) scan of surface morphology and a Kelvin Probe Force Microcopy (KPFM) scan of surface potential. These measurements are taken using a Kelvin probe, basically a measure of surface-to-tip capacitance.

How the AFM scan is taken is by a suspended tip, which features a Kelvin probe on the underside of a cantilever, closely approached to the surface of the material without making contact. The tip oscillates at a set frequency and when it encounters interactive forces from the surface, indicative of topography changes, the laser is deflected away from the center of the quadrant photodetector. The deflection happens as an adjustment to balance out the tunneling current. The tip adjusts its frequency in amplitude or phase until the laser is repositioned[2]. These changes are recorded and shown in real time as the scan runs over a preset area.

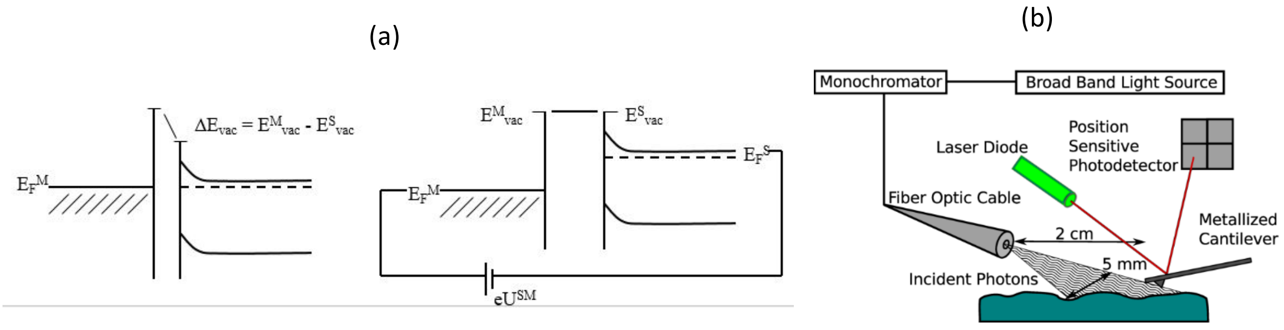

Figure 2: Experimental Setup: (a) Depiction of KPFM circuit (b) Full setup including components for SPS, AFM, and KPFM

Simultaneous to AFM being recorded, KPFM runs at a resonant frequency in order to track the potential at the surface. The second frequency follows an applied AC voltage between the sample and the cantilever. The KPFM measures the difference in work function between the probe tip and the sample surface. A work function is the energy needed to eject electrons from the surface (E_{vac}) by overcoming the barriers placed upon them in the conduction band. The tip material is meant to be made of a substance of with a stable work function so when slight variation is measured it can be attributed to changes in the Fermi level position within the semiconductor material. When two materials come into close proximity each material's Fermi level align to the same position as seen in the leftmost diagram in Figure 2(a), but the vacuum level (E_{vac}) of each is different. This difference creates an electric field between the sample and the metal tip, thus creating an excess of negative charge on the sample (n-type band bending) and positive charge at the tip. As the tip oscillates closer to the material, the electric field increases. The circuit shown on the right of Figure 2 (a), shows an applied feedback voltage that nullifies the current flow. This is the measurement taken during KPFM.

Figure 2 (b) displays additional components used for taking SPS data in conjunction with KPFM and AFM. A broad band light source, essentially a source encompassing all wavelengths of light, is feed into a monochromator, which is a device that can separate those wavelength which correspond to a certain energy that photon possesses. The separated light is feed into a fiber optic attached on the microscope to direct light to the sample surface. When the light hits the surface electrons can get excited and jump to a higher energy state. Software track the contact potential difference verses photo energy in real time. The purpose of the two part scan is to relate defect states to the sample structure in order to synthesis defect free materials.

---

[2] Ed Fei and Ryan Brock, "Park XE-70 AFM User Manual"

Results and Discussion

Data collection began with $Mg_{44}Zn_{56}O$, an alloy of 56 % zinc and 44% magnesium, in order to become familiarized with the equipment and method. An alloy of ZnO was chosen because it is a well-defined material: its defect and bandgap energies, n-type behavior, large excitation binding energy, and bright luminous. Figure 3 shows three SPS graphs of a sample of $Mg_{44}Zn_{56}O$. Graphical interpretation of direction of the slope at the peaks and valleys represents changes in the work function. ΔCPD is the negative sign of work function. In an n-type material like ZnO as band bending decreases, the work function also decrease. This is represented graphically as an increase in ΔCPD. The band gap energy is measured to be between around 3.9 eV. Defect states were measured to be at 1.7 eV and 2.2 eV which makes sense since the populating and depopulating states add up to the band gap. Energies of the defects are shifted as seen left to right of the graphs in figure 3 because of issues dealing with possible charging. This data was taken successively without any breaks in between. This could have led to electrons not having enough time to settle in to states before they were excited again.

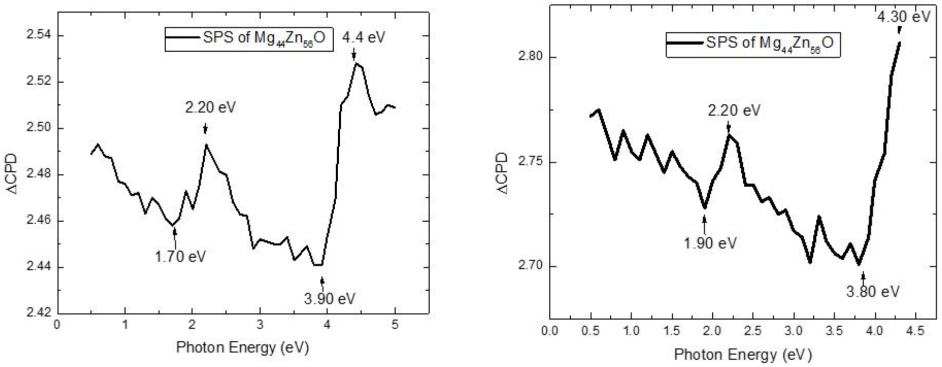

Figure 3: $Mg_{44}Zn_{56}O$ data from June 13, 2016. Shows band gap energy on average between 3.8 eV and 4.3 eV (the true bandgap energy lies somewhere in between these numbers). At $h\nu = 1.7$ eV, there is an increase in surface state electrons (populating a state) related to an increase in work function and band bending. At $h\nu = 2.2$ eV, there is a decrease in surface state electrons (depopulating a state) related to a decrease in band bending and work function.

Pervious experimentation which reported methyl-terminated germanane, $GeCH_3$, as having a p-type response and conductive. Figure 4 shows collected data that shows this behavior. Band gap energy is measured to be between 1.7 eV and 1.8 eV which is congruent to expectation of the band gap energy around 1.76 eV. Figure 4(a) shows at $h\nu = 0.95$ eV, electrons are excited to the negative depletion region, increasing the negative surface charge, thus an increase in band banding and a decrease in work function. At $h\nu = 1.2$ eV, that same state is depopulated into the conduction band resulting in less band bending. Figure 4(b) was taken on the same day and shows a similar but shifted spectra, this could be due to the charging issue saw in the $Mg_{44}Zn_{56}O$ spectra.

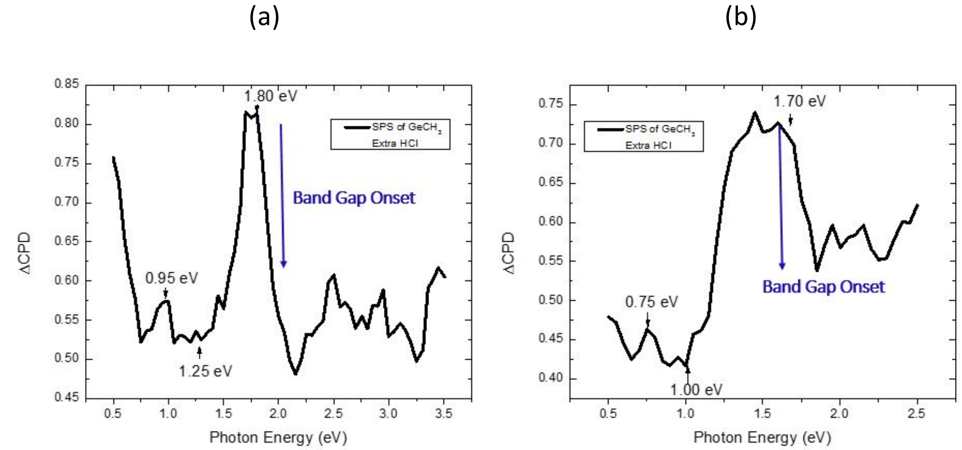

Figure 4: $GeCH_3$ P-Type data from July 12, 2016: (a) Defect states at 0.95 eV and 1.2 eV. Band gap from 1.80 eV to 2.20 eV (b) Defect states at 0.75 eV and 1.0 eV with band gap at 1.7 eV

Study of methyl-terminated germanane also showed an n-type behavior which did not correlate with pervious experimentation. Figure 5 shows data collected on the same batch of $GeCH_3$ flakes but an earlier sample. The bandgap energy is approximately 1.6 eV. There is a defect state, similar to p-type graphs, at 0.8 eV.

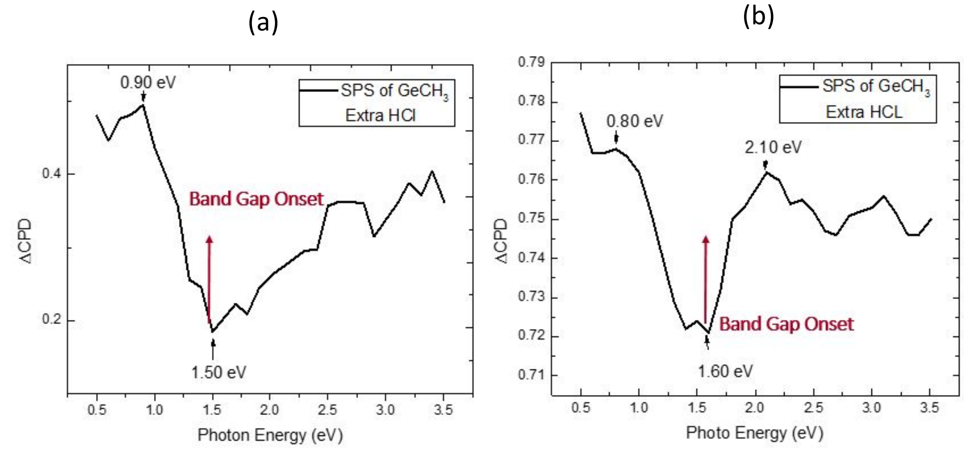

Figure 5: $GeCH_3$ N-Type data: (a) June 17, 2016, Defect state at 0.9 eV with band gap at 1.5 eV (b) June 21, 2016, Defect state at 0.8 eV with band gap at 1.6 eV

The interpretation of this data could suggest that methyl-terminated germanane contains both n-type and p-type characteristics. N-type and p-type conductivity has also been seen in monolayer MoS_2[3]. Many factors and issues could have also attributed to the diverse data collection such as oxidation. Over time $GeCH_3$ begins to oxidize, signified by the flake turning yellow, therefore the equipment takes data on both $GeCH_3$ and GeO_2. The equipment is also a factor because it has sensitives to temperature, vibrations, dust and humidity. Nosie is often the resultant of subtle

---

[3] Kapildeb Dolui, Ivan Rungger, Stefano Sanvito "Origin of the n-type and p-type conductivity of MoS2 monolayers on a SiO2 substrate"

variations during data collection. The nature of the material because it has been noted that the Ge family provides a characteristically low signal when put under testing.

Conclusions

This investigation has demonstrated the defect states and characteristics of 2D Methyl-Terminated Germanane ($GeCH_3$). The data collected determines that $GeCH_3$ has a duality shown through having both a p-type and an n-type behavior. The response of the data could be attributed to a variety of factors such as oxidation and humidity, therefore continued testing of this material with consistent results is required. This has significant future implications for relating these behaviors to sample structure in order to synthesize materials without defects.

Acknowledgments

Research for Undergraduates (REU) program is funded by NSF and hosted by Center of Emergent Materials at The Ohio State University. Acknowledgments to all group members of the Brillson group for assistant in this research.

Footnotes, Endnotes and References

1. Kapildeb Dolui, Ivan Rungger, Stefano Sanvito “Origin of the n-type and p-type conductivity of MoS2 monolayers on a SiO2 substrate”; (11 Jan 2013)
2. L. Kronik and Y. Shapira, Surface photovoltage phenomena: theory, experiment, and applications, Surf. Sci. Repts. 37, 1 (1999).
3. Shishi Jiang, Sheneve Butler, Elisabeth Bianco, Oscar D. Restrepo, Wolfgang Windl, and Joshua E. Goldberger “Improving the stability and optical properties of germanane via one-step covalent methyl-termination” (25 Feb 2014)
4. Leonard J. Brillson “An Essential Guide to Electronic Materials, Surfaces, and Interfaces” (2016)

My Summer REU Paper

Gate Dependent Transport and Scanning Tunneling Microscopy of a Graphene Device

Ryan Rodriguez, Grady Gambrel, Jay Gupta Ph.D.
Ohio State University Physics Department, Center for Emergent Materials, Lawrence Technological University

ABSTRACT

Graphene, recognized as a two dimensional (2D) hexagonal lattice of carbon atoms, presents interesting electrical properties that show potential in electrical applications. The goal of this research is to provide characterization data for 1 micron wide gated graphene sheet and the scanning tunneling microscopy/spectroscopy (STM/STS) investigation of the electron transport for cobalt coated graphene devices. Graphene will be analyzed using atomically resolved scanning tunneling microscopy while a back gate voltage is applied to shift the Fermi level. The resistance of uncoated graphene will be measured with respect to the back gate voltage applied. We provide a method for navigate to small (< 10 micron) wide graphene via capacitance navigation as well as transport data for graphene at ultra-high vacuum pressures.

I. Background and Introduction

Graphene is recognized as a 2D hexagonal lattice of carbon atoms with a 2.46Å lattice spacing (figure 1), where the carbon atoms are located at each vertex of the hexagon and forms covalent bonds with the three neighboring carbon atoms.

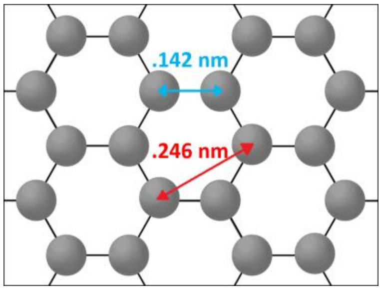

FIG 1. Atomic structure of Graphene. Carbon atoms form hexagonal lattices by forming covalent bonds with three adjacent atoms.

Graphene can be manipulated into other dimensional forms, for example a graphene sheet can be rolled into a 1D nanotube, but 2D graphene sheets have the simplest electronic spectra [6,7]; they are considered to be zero-gap semiconductors, characterized by an uncommon band structure found in electron energy/momentum space. Unlike insulator which have large electronic band gaps, and metals with overlapping bands, Graphene has no band gaps and no overlapping bands, which causes it to have strong conduction properties. Figure 2 shows the band structure of graphene recreated in Energy/Momentum space. The geometry will resemble two circular cones (figure 2). The Dirac cones has no gap between them unlike insulators, and no partially filled cones, unlike metals. The structure of the Dirac cones make graphene a promising candidature for tunable electronic devices.

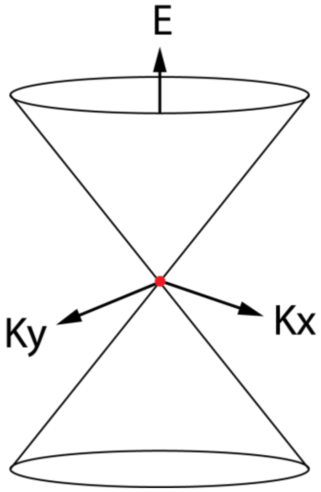

FIG 2. Dirac Cones in energy/momentum space. The energy bands of graphene can be represented as conical sections, labeled "Dirac Cones" by plotting electron energy as a function of time. There is no gap between the top cone (conduction bands) and bottom cone (valence Band), unlike insulators. The top cone is also not filled, unlike a metal. The boundary of the cones represent the spaces of electron orbitals. At the Dirac point, available electron orbits approach zero, causing conductivity to approach zero.

By placing an insulator between a graphene and conductive sheet and applying a back-gate voltage between the two, a perpendicular electric field is applied to graphene, causing the top Dirac Cone to be filled with additional electrons; the resulting increase in the conduction band causes an increase in conductivity. By relating resistivity, conductivity, and back-gate voltage, we can analyze electron transport using resistance and back-gating voltages.

Since graphene is considered to be a semi-metal due to its zero gap band structure, analysis of surface state changes may present new comprehension of cobalt covered graphene surface interactions. While transport measurements can offer useful information regarding Fermi level tunability in graphene, simultaneous transport and STM/STS measurements can provide a more area specific understanding of the Density of States (DOS) tunability. Previous research has already demonstrated that gate tunable graphene devices can be fabricated with [1], and further research show that a tunable back-gate voltage with scanning tunneling microscopy (STM) analysis can be used to investigate electrical state changes in graphene [2]. Recent studies have been conducted into the surface state and electrical properties of graphene deposited on various material substrates [2-3, 9-13], however, research of the surface state and electronic properties of sub-10 micron wide covered graphene strips has been minimal [14]. A greater understanding of sub-micron sized devices can lead to better innovation in electronics. In this paper, we provide transport data, represented by resistance versus back-gate voltage data, for pre and post annealed graphene devices. In this paper we present transport data for uncoated and cobalt-coated graphene. We also provide local STM and STS measurements for each.

II. Methods

The 10 to 1 micron graphene geometry was grown using a chemical vapor deposition method (CVD) onto copper substrate. The copper is heated to near its melting point, where it is then exposed to hydrocarbon gas. The hydrocarbon gas catalyzes on the copper to form graphene [3]. The graphene was transferred from copper to a Silicon (Si) wafer with a 300nm SiO2 insulating film between the two using polymethyl methacrylate (PMMA) to stabilize the single layer graphene [8]. The CVD graphene is patterned with six Au electrodes to make electrical contact, assist with STM navigation and transport

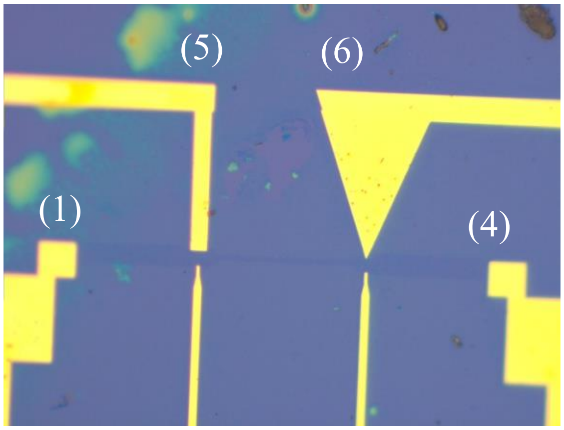

Fig 3. Four gold electrodes were deposisted on top a 10 micron to 1 micron wide graphene sheet depsoted on SiO2 wafer. (seen as dark blue) Electrodes are labeled 1,4,5,6.

measurements. The Au electrodes are labeled one through six, as seen in figure 3. For this research, we used only leads 1,4,5,6. Resistance measurements are recoded using a 2 point contact approach. An additional back-gate voltage was applied to the Si wafer through the Cu sheet. After patterning, the graphene is wired to sample holder. Once the device is connected, preliminary table top measurements are made to establish that a complete circuit has been made through the graphene by plotting current as a function of voltage. A constant slope will indicate a complete circuit. Graphene resistance versus back-gate voltage measurements were taken to establish a base line before transferring to vacuum chamber for baking and current annealing. The graphene device is baked at approximately 370 Kelvin (K) in the load lock (LL) of the STM chamber to remove any adsorbates that may have formed on the surface of the graphene strip. The graphene is then moved into the preparation (prep) chamber of the STM for current annealing. The annealing process begins with a small DC voltage applied across the graphene strip. The applied voltage is increased between 0.1 to 1v steps until the current is found to decrease as a function of time. Past research has reported that a step exponential decay followed by saturation [4], however we report a small linearly decreasing current rate. The current annealing process is included to shift the Dirac peak to a lower gate voltage. Once the Dirac peak is lower to a satisfactory Vg, the temperature dependence was tested. Liquid Nitrogen (LN_2) was driven through STM manipulator arm to lower the graphene device temperature to around 80 K. The device temperature was then allowed to rise to room temperature. After measurements, the device is moved into the low temperature STM (LT-STM) operating 5K for analysis.

Topographic imaging through STM is achieved by applying a functional bias between sample and conductive tip. The current function is measured as tip scans across the sample surface. At close proximities, the probe and sample wave functions will begin to overlap, allowing electrons to tunnel between the sample and tip, creating a tunneling current. The tunneling current can be related to tip height by the equation

$$I \propto e^{-\frac{2s}{\hbar\sqrt{2m\phi}}} \quad (1)$$

Where s is the barrier width (tip to sample separation), m is electron mass, and ϕ is barrier height. As the s increases, the tunneling distance will decrease exponentially.

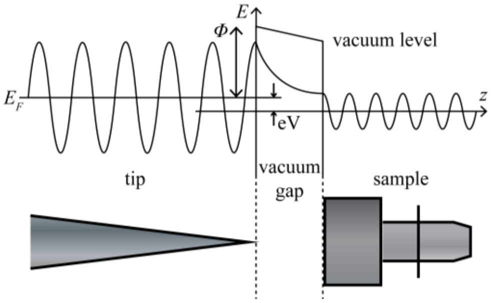

FIG 4. Barrier in vacuum STM. The potential barrier between tip and sample energies is caused by the vacuum space. For electrons to tunnel from tip to sample, there must empty energy levels in the sample that match the levels in the tip. Tunnel current will depend on the density of states in sample and electrons in the E_F – eV to E_F range [13].

The STM can operates using two methods, constant current or constant height mode. In constant current mode, the STM uses a feedback loop to extend or retract the tip to maintain a constant current through the tip-sample interface. The change in tip height is used to reconstruct a topographical image. Constant height maintains a constant height and records current changes to provide images. Lastly, STM can also provide tunneling spectroscopy.

Tunneling spectroscopy (STS) is achieved by hold the STM tip in a singular locations while measuring current as a function of applied voltage. The dI/dV measurements provide information on local DOS and the associated band structure of the material being scanned. STS measurements with simultaneous transport data offers a more detailed investigation of the tunabiltiy of graphene.

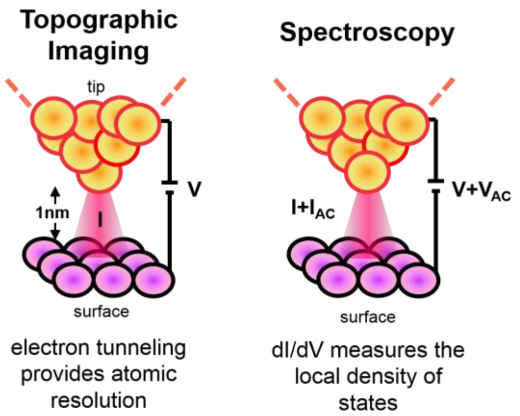

FIG 5. Schematic view of STM and STS. STM uses DC voltage bias to measure tunneling current to achieve atomic resolution. STS uses a DC voltage bias plus an additional AC modulation. STS uses dI/dV measurements to probe the local density of electronic states

In order to navigate the STM tip to the 1 micron wide graphene strip, a capacitance method is used. The capacitance navigation method uses two bias voltages applied to the STM, one voltage for the tip and one for the back-gate voltage [5]. The typical tunneling current used in STM is

$$I = G_T V_s \quad (2)$$

With V_s as the bias voltage to the sample, and G_T as the tunneling conductance. To take measurements, an AC voltage (V_s^*) is applied to sample voltage bias so that an AC current (I*) is applied to the STM tip.

$$I^* = G_T V_s^* + i\omega C V_s^* \quad (3)$$

The AC current in (3) is formed by two components, the first term from the electron tunneling, and the second term from the pickup capacitance (C) which can be considered the capacitance between the STM tip and sample.

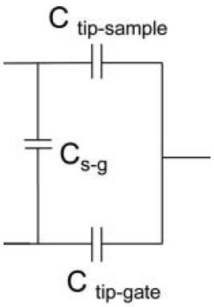

FIG 6. Equivalent circuit of STM Tip, graphene sample, and back-gate capacitance. Capacitance is formed when an AC signal is sent to the STM tip. $C_{tip-sample}$ will short out when the tip is no longer above the sample.

Since the pickup current is dependent on the sample geometry and can be easily distinguished from the tunneling current, it can be used to precisely monitor tip navigation [5]. Capacitive current will peak near the center of the sample, so by plotting the spatial derivatives dI/dx, dI/dy, and position, one can identify the edges by finding the turning points of the plot (figure 7).

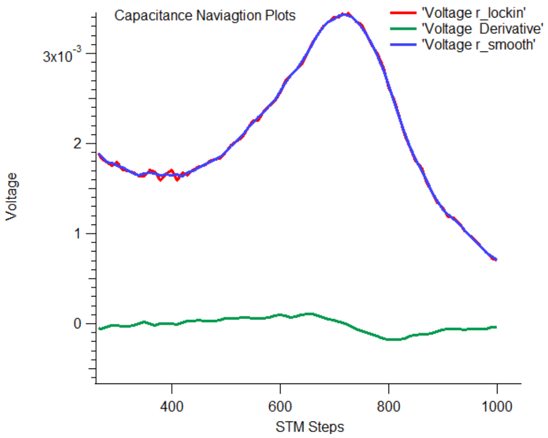

FIG 7. Spatial derivative of feedback capacitance of conductive sample. The turning points of the green plot indicate edges of the sample. Through edge detection, the STM tip can be navigated across small sample spaces

Once the edges are found, the tip can be navigated to the desired scanning area depending on the device geometry.

The STM probe tip will be positioned to the 1 micron wide graphene strip to begin data collection. Graphene resistance vs back-gate voltage measurements will be taken at 5 K.

The resistance can be related to the local DOS and topographical changes taken by STM/STS. Changes in DOS can thus be related to electron transport in graphene.

III. Results and Discussion

After baking at approximately 100 ° C for three hour at a base pressure of 10^{-7} mbar, we report seeing a Dirac peak at 5v back-gate voltage (Vg) with a base resistance of 140 Kohms at Vg = 0v. The graphene device was placed in the preparation chamber with base pressure of 10^{-11} mbar for additional current annealing lasting 2 hours, we report a clear Dirac peak at Vg = 0.5v with peak resistance at 185 Kohms and a base resistance at 181.5 Kohms at Vg = 0v. We report that the baking process was the most beneficial for improving the Dirac peak detection.

After current annealing, the graphene sample was cooled with LN_2 to 80 K and reheated to room temperature while transport data was taken. An 8 kohm increase was detected in peak resistance as the sample temperature decreased as shown in figure 8.

After transferring the uncoated graphene device to the STM chamber, we repeated Dirac Peak measurements. We report a Dirac Peak shift to the -5 to -6 back-gate voltage range (See figure 9). We believe this shift of peak location can be attributed to the graphene device being coated with a small amount of adsorbates while the graphene was stored in the STM prep chamber.

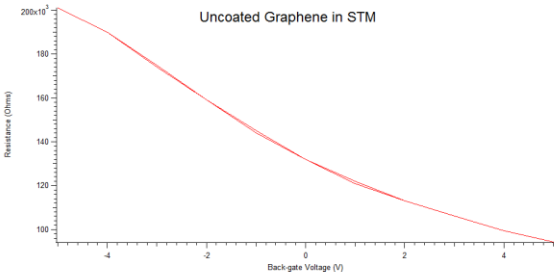

FIG 9. Dirac peak measurements for uncoated graphene. The Dirac peak measurements in the STM chamber show that the peak shifted into the -5 to -6 Vg range. The peak resistance was measured at around 200 kohms.

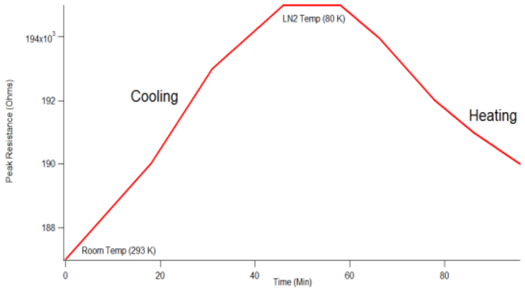

FIG 8. Dirac Peak resistance versus time cooling/heating curve. The Dirac peak resistance versus back-gate voltage was measured multiple times while the device was cooling to about 80 K and while warming to room temperature (290 K). The time of each measurement was recorded. The figure provided shows peak resistance changes with respect to time. The center plateau indicates that the sample has reached LN_2 temperatures.

IV. Conclusions

In conclusion, we have provided a thorough investigation of 10 to 1 micron sized graphene grown on SiO2. The local density of electron states was measured via Dirac peak detection and related to local transport measurements before and after the current annealing process. We report our current annealing/baking process as an effective method for shifting Dirac peak voltage closer to zero voltage point. As for graphene temperature dependence, our transport measurements show that a cooling effect will result in an increased resistance peak, with no effect on the peak voltage. These results are expected as a lower temperature will limit the amount of transporting electrons, as is similar to semiconductors. This shows promising research for temperature dependent studies above room temperature as well as research into transport measurements for graphene coated with metal.

We observed a Dirac peak gate voltage shift of -5.5 volts when the graphene was transferred to the STM chamber.

Capacitance navigation shows promising results to locate small graphene devices to further investigate topological changes in graphene when coated with cobalt and tuned via a back-gate voltage.

V. Acknowledgments

The REU program is part of an NSF Materials Research Science and Engineering Center (MRSEC) supported under NSF Award Number DMR-1420451.

We would also like to thank Grady Gambrel and Dr. Jay Gupta for their support and helpful discussions.

VI. Footnotes, Endnotes and References

1 Jung, H. S., Tsai, H. Z., Wong, D., Germany, C., Kahn, S., Kim, Y., *et al.* Fabrication of Gate-tunable Graphene Devices for Scanning Tunneling Microscopy Studies with Coulomb Impurities. *J. Vis. Exp.* (101), e52711, doi:10.3791/52711 (2015).

2 Alexander Riss *et al.*, "Imaging and Tuning Molecular Levels at the Surface of a Gated Graphene Device," ACS Nano 8 (6), 5395-5401 (2014).

3 Qingkai Yu *et al.*, "Control and characterization of individual grains and grain boundaries in graphene grown by chemical vapour deposition," Nat Mater 10 (6), 443-449 (2011).

4 J. Moser, A. Barreiro and A. Bachtold, "Current-induced cleaning of graphene," Appl.Phys.Lett. 91 (16), 163513 (2007).

5 Guohong Li, Adina Luican and Eva Y. Andrei, "Self-navigation of a scanning tunneling microscope tip toward a micron-sized graphene sample," Rev.Sci.Instrum. 82 (7), 073701 (2011).

6 Novoselov, K. S. *et al.* Electric field effect in atomically thin carbon films. *Science* **306,** 666–669 (2004).

7 B. Partoens and F. M. Peeters, "From graphene to graphite: Electronic structure around the K point," Phys.Rev.B 74 (7), 075404 (2006).

8 Ji Won Suk *et al.*, "Transfer of CVD-Grown Monolayer Graphene onto Arbitrary Substrates," ACS Nano 5 (9), 6916-6924 (2011).

9 J. Baringhaus *et al.*, "Local transport measurements on epitaxial graphene," Appl.Phys.Lett. 103 (11), 111604 (2013).

10 Jeroen B. Oostinga *et al.*, "Gate-induced insulating state in bilayer graphene devices," Nat Mater 7 (2), 151-157 (2008).

11 Yujie Ren *et al.*, "Controlling the electrical transport properties of graphene by in situ metal deposition," Appl.Phys.Lett. 97 (5), 053107 (2010).

12 R. S. Shishir *et al.*, "Theory and measurements of room temperature transport in graphene using SiO2 backgate and electrochemical gate," Journal of Vacuum Science & Technology B 27 (4), 2003-2007 (2009).

13 Anonymous "Scanning tunneling microscopy", [http://www.maths.tcd.ie/~bmurphy/thesis/thesisse3.html#tailthesisse3.html], 2016 (7/8/2016).

14 1 S. J. Tjung, S. M. Hollen, G. A. Gambrel, N. M. Santagata, E. Johnston-Halperin, J.A. Gupta, "Crystalline hydrogenation of graphene by tip-induced field dissociation of H2
", In Preparation, .